J Mater Sci (2017) 52:9477–9490

Chemical routes to materials

Enhanced visible-light photocatalytic activity from graphene-like boron nitride anchored on graphitic carbon nitride sheets

Hang Xu[1,2], Zhang Wu[1,2,*], Yueting Wang[1,2], and Chenshuo Lin[1,2]

[1] *Key Laboratory of Integrated Regulation and Resource Development on Shallow Lake of Ministry of Education, College of Environment, Hohai University, Nanjing 210098, China*

[2] *College of Environmental Science, Hohai University, Nanjing 210098, China*

Received: 8 March 2017
Accepted: 3 May 2017
Published online: 9 May 2017

ABSTRACT

Visible-light-driven, graphene-like boron nitride (g-BN)-mediated graphitic carbon nitride (g-C_3N_4) photocatalysts were firstly synthesized via a facile and green method. The as-prepared catalyst samples were characterized by their morphology, optical and electrochemical performance. The photocatalytic activity of the g-BN/g-C_3N_4 composites was evaluated by bisphenol A photodegradation and H_2 evolution under visible-light irradiation. The results indicated that 0.9% g-BN/g-C_3N_4 exhibited the best photocatalytic activity amongst the hybrid photocatalysts. The enhanced photocatalytic activity was ascribed to excellent surface properties, an enhanced visible-light harvesting capability, a stable structure and a high-efficiency separation rate of photoinduced electron–hole pairs. This work will support the rational design of g-BN-based photocatalytic materials for use in energy conversion and environmental preservation.

Introduction

Visible-light-driven photocatalytic reactions are a favourable solution to help resolve rising ecological and energy affairs [1–3]. From the perspective of solar energy applications, the sunlight absorption capacity of semiconductors and the reaction efficiency of photogenerated charge carriers influence photocatalysis. Amongst various semiconductor photocatalysts, metal-free graphitic carbon nitride (g-C_3N_4) has emerged as one of the most prominent photocatalysts due to its high earth-abundance, non-toxicity, thermal and chemical stability. However, pristine g-C_3N_4 has poor yields for H_2 production and a low efficiency for degradation of pollutants under visible-light irradiation [4].

Additionally, g-C_3N_4 exhibits low photocatalytic activity because it supports a narrow visible-light response range, low surface area, slow charge transport and fast charge recombination [5]. Several investigations have been undertaken to overcome

Address correspondence to E-mail: hohaiwuzhang@126.com

DOI 10.1007/s10853-017-1167-6

these disadvantages. A useful strategy to develop the photocatalytic activity of g-C_3N_4 is to couple it with precious metal nanoparticles [6, 7]. The improved activity is credited to the favourable charge transport properties and high visible-light absorption, which is due to the surface plasmon resonance (SPR). Constructing semiconductor heterojunctions with other photocatalysts, such as TiO_2, AgO, ZnO, BiOCl, BiOBr, BiOI [8–13], is also a favourable prospect. The heterojunction system can optimize light harvest and effectively enhance the separation of photoexcited electron–hole pairs. However, drawbacks of characteristic heterojunctions include limited high charge separation efficiency and a strong redox ability of photogenerated holes. The topmost issue with these composites is the discharge of toxic metals during the course of photocatalytic processes. Recently, cationic-modified g-C_3N_4 was found to have a stronger photocatalytic ability because of improved electron–hole separation performance via an interface charge transfer effect [14]. However, the stability of photocatalysts is instinctively poor. Another approach to modify g-C_3N_4 is utilize the high oxidation ability of redox pairs [15, 16]. Photocatalytic systems that are dependent on metal-free, viable resources are predominantly necessary for large-scale photocatalytic applications.

The rapid development of graphene-layered materials has gained substantial interest in current times [17]. 2D photocatalysts coupling with metal-free nanomaterials such as GO have been proved the improved photocatalytic activity [18, 19]. The coupling of g-C_3N_4 with metal-free nanomaterials, such as carbon nanotubes [19] and graphene [20–22], has received considerable attention because this material demonstrates remarkable features that include a large specific surface area, improved elasticity, tough mechanical strength and extraordinary electronic properties. The photocatalytic ability is distinctly improved through this process. Boron nitride (BN), which is a remarkable representative of a 2D crystal, exhibits remarkable properties that include a small dielectric constant, increased thermal conductivity and tough mechanical strength. This material can be employed as a solid-state lubricant, electronic device or a filler material in composites [23–27]. Additionally, the photocatalytic activity to degrade pollutants was significantly enhanced. Specifically, the structures of graphitic carbon nitride (g-C3N4) and graphene-like BN are similar to the graphene and they have the good performance of graphene-like structure. The infusion of BN can ultimately enhance the photocatalytic activity by modifying the light absorption or subduing the recombination of photoexcited electrons and holes. Graphene-like BN is a material with fewer layers and a wide surface. The modification of a layered or high surface area material can effectively reduce the rapid recombination of photogenerated electron–hole pairs in the original photocatalyst during photocatalysis [28–31]. Therefore, combining a graphene-like BN architecture with a vastly effective photocatalyst is critical to withstand energy and environmental recommendations.

Our work has produced a source of rich metal-free g-BN/g-C_3N_4 composites that were created by glazed ultrasonic stripping of a g-BN thin sheet directly onto the surface of an ultrasonic stripped g-C_3N_4 thin sheet. The g-BN covered g-C_3N_4 composite demonstrated a highly improved photoreaction rate for bisphenol A mineralization with visible-light illumination compared with g-C_3N_4 and H_2 production. The composites are more economic and green than other metal-free components for modification of g-C3N4 [32]. The role of g-BN in the composite was thoroughly investigated. Because the g-BN/g-C_3N_4 composite possesses metal-free and ecology-friendly properties, it is a favourable photocatalytic system for practical applications.

Experimental section

Synthesis of the photocatalysts

Preparation of g-C_3N_4

A simple calcination method was used to prepare pure g-C_3N_4, as described in the literature [33]. Urea was boiled in static air to 520 °C (ramp rate 2 °C/min) in a quartz boat and allowed to cool for 4 h. The yellow g-C_3N_4 product was gathered and milled to a powder with an agate mortar for further use.

Preparation of g-BN

Calcinations were conducted to prepare graphene-like BN using boric acid and urea as reactants. Boric acid and urea were dissolved in 40 ml of distilled water at a mole ratio of 1:24. This solution was heated at 80 °C to obtain a white solid. This solid was then

calcined at 900 °C for 5 h in a nitrogen atmosphere [34].

Preparation of the g-BN/g-C_3N_4 nanocomposite

The g-BN/g-C_3N_4 nanocomposite was typically prepared utilizing the following method. A quantity of g-C_3N_4 (0.2 g) was dispersed in 30 ml ultrapure water and this mixture was called A suspension. A specific mass of graphene-like BN was added to 10 ml of ultrapure water and this mixture was called B suspension. The two suspensions were sonicated for 10 h. Later, the solutions were combined and vigorously stirred for 24 h, after which the solvent was vaporized at 100 °C and grinded for 30 min. The resulting powder was calcined at 350 °C for 2 h. This process was followed by synthesizing various mass fractions of g-BN/g-C_3N_4 materials with 0.3, 0.6, 0.9 and 1.2% g-BN, respectively.

Characterization

X-ray diffraction (XRD) was used to ascertain the crystal phase structures of the samples (Bruker, D8) using Cu Kα ($\lambda = 0.15418$ nm) radiation. The scan range of 2θ was 10°–90°. Field emission scanning electron microscopy (FE-SEM, Hitachi, S-4800) and transmission electron microscopy (TEM, JEOL, JEM-2010) were employed to inspect sample morphology. Fourier transform infrared (FTIR) spectra were performed using a Niconet 5700 FTIR spectrometer by dispersing the samples in a KBr desiccant in the range of 400–4000 cm^{-1}. K-alpha X-ray sources (USA) were used for X-ray photoelectron spectroscopy (XPS) measurements. A spectrophotometer (TU-1901) was utilized to record UV–Vis diffuse reflectance spectra (UV–Vis DRS) with $BaSO_4$ as the reflectance standard. Additionally, a FluoroMax-4 spectrofluorometer (HORIBA, USA) was used to collect the photoluminescence (PL) spectra of the as-prepared samples with an excitation wavelength of 400 nm. N_2 adsorption–desorption isotherms were used at 77 K along with an ASAP2020HD88 instrument to record specific surface areas and pore structures of the as-fabricated samples. An Apollo9000 TOC analyser was employed to conduct total organic carbon (TOC) tests. A Bruker model A300 spectrometer was utilized to determine the EPR spectra. Furthermore, a BAS Epsilon Electrochemical System was used to perform photo-electrochemical measurements under visible-light irradiation with a conventional three electrode cell immersed in a 50 ml solution of 0.2 M Na_2SO_4 (pH 6.8). The sample electrodes that were fabricated on indium–tin oxide (ITO) conductor glasses were used as the working electrodes. Powder samples (8 mg) were dispersed in 500 μL of ultrapure water with 50 μL of 5% Nafion solution with sonication to obtain a slurry mixture. The ITO glasses were initially washed by sonication with ultrapure water, acetone and ethanol for 30 min. A side section of the ITO glass was first secured with tape, after which the slurry was spread onto the glass. The working electrode was dried overnight under ambient conditions. A saturated calomel electrode (SCE) and Pt wire were considered as the reference and counter electrode, respectively. A 300 W Xe lamp was utilized as the excitation light source combined with a visible-light filter ($\lambda > 420$ nm). The light source was at a distance of 1 cm from the photo-electrochemical cell (Fig. 1).

Photocatalytic performance evaluation

Photooxidation of a bisphenol A solution (10 mg L^{-1}) was conducted to assess the photocatalytic performance of the as-prepared photocatalysts. This experiment was conducted in a circulating water supply system where the temperature was maintained at 20 °C. Then, the catalyst (50 mg) and the biophenol A solution (50 ml) were combined. The process of ultrasonification was performed to suspend the powders before adding the catalyst into the model wastewater. The suspension was magnetically mixed for 30 min in a dark environment before illumination to maintain the adsorption–desorption equilibrium of biophenol A. The suspension was then illuminated with a cut-off filter (<420 nm) and an irradiation intensity of 100 mW cm^{-2} using a 300 W Xe lamp. Aliquots of the irradiated suspension were gathered, centrifuged and examined on an Aligent 1260 high-performance liquid chromatography (HPLC) system. A mobile phase of methanol–water (70:30) with a 40-mL injection volume and a flow rate of 1 mL/min was also utilized for this experiment. Detection was achieved with a scanning fluorescence detector (Waters 474). The analysis wavelength was 278 nm. The retention time under these conditions was 4.68 min. A Shimadzu TOC-VCBH Total Organic Carbon (TOC) analyser was used to analyse the degree of mineralization. The removal of catalyst

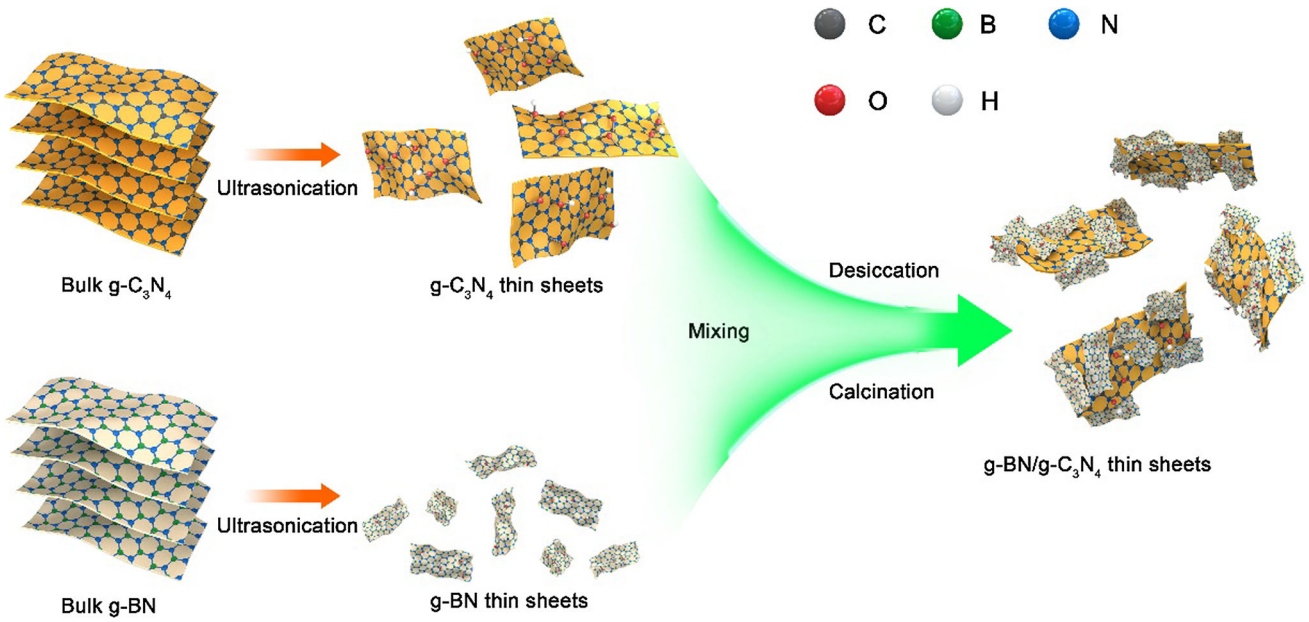

Figure 1 Schematic representation for the synthesis of g-BN/g-C_3N_4 thin sheets.

particles was performed by gathering the total organic carbon (TOC) from the reaction suspension in preset time intervals and filtering them through a membrane filter (Sartorius, 0.45 μm).

Photocatalytic water-splitting test

The visible-light-induced H_2 production reaction was performed in an online photocatalytic hydrogen production system (LbSolar-3AG, PerfectLight, Beijing). The photocatalyst (0.05 g) was mixed with an aqueous solution (90 mL of water and 10 mL of whole sacrificial agent), after which the co-catalyst Pt nanoparticles were added via an in situ photodeposition method. Later, a specific quantity of H_2PtCl_6 $6H_2O$ aqueous solution was fused via droplets into the system to produce Pt on the surface of the photocatalyst. The solution was degassed multiple times to eliminate the air before the irradiation process. The process of irradiation was then conducted using a 300 W Xenon lamp (CEL-HXF300, PerfectLight, Beijing) with an optical filter ($\lambda > 420$ nm). Cold water was illuminated with visible-light to maintain the reaction solution temperature at 10 °C. An online gas chromatograph was used to identify the photocatalytic H_2 evolution rate (GC D7900P, TCD detector, Ar carrier, 5A molecular sieve column).

Results and discussion

Morphology characterization

Scanning electron microscopy (SEM) analyses (Fig. 2b) revealed that in the g-BN/g-C_3N_4 hybrid, a large film-like g-BN material coated the surface of the g-C_3N_4 nanosheets with a high dispersion, whereas pure g-C_3N_4 showed a smooth and clean surface (Fig. 2a). The results confirmed the formation of the hybrid. Notably, graphene-like BN preferably coats the uneven g-BN/g-C_3N_4 surface area, as shown by the less graphene-like BN coating on the smooth area of g-BN/g-C_3N_4 surfaces. As shown in Fig. 2c, d, HRTEM images of 0.9% g-BN/g-C_3N_4 depict graphene-like BN and a layered structure that provides a substrate for g-BN. HRTEM results point to the existence of graphene-like BN that created close interfaces in the composite samples, which can enhance the charge separation and photocatalytic efficiency. The combination of g-BN and g-C_3N_4 in the composited 0.9% g-BN/g-C_3N_4 sample was confirmed by the energy-dispersive X-ray spectroscopy (EDS) elemental mapping images, which substantiate the uniform distribution of C, N and B throughout the 0.9% g-BN/g-C_3N_4 structure at a nanoscale (Fig. S1).

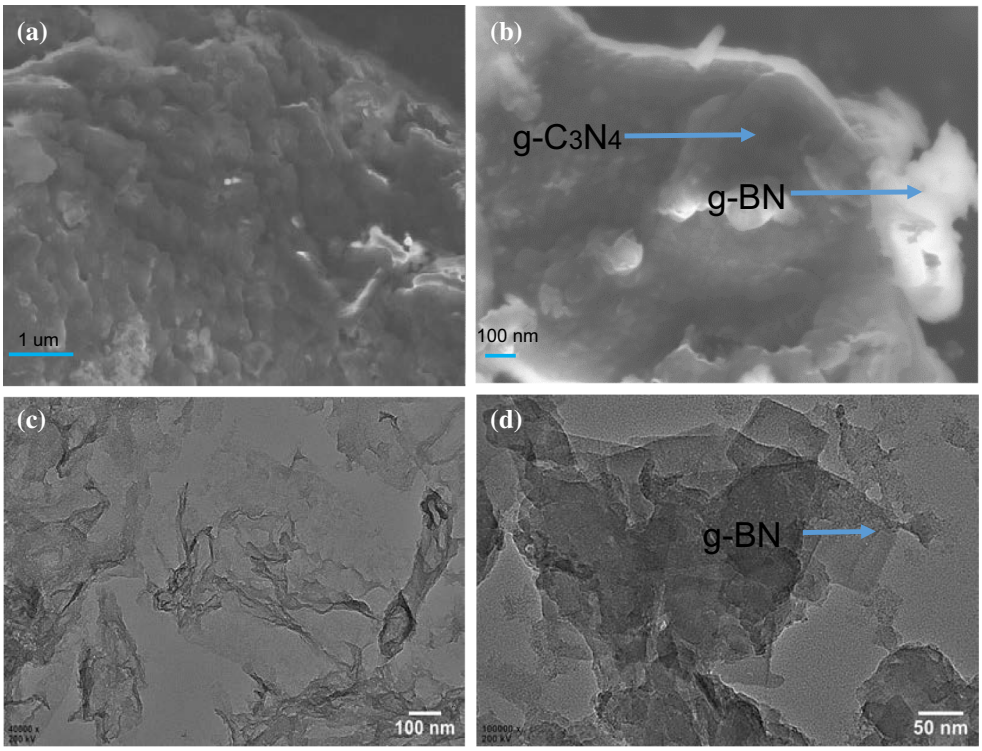

Figure 2 FESEM **a** pure g-C_3N_4, **b** 0.9% g-BN/g-C_3N_4 and HRTEM images of **c** pure g-BN and **d** 0.9% g-BN/g-C_3N_4.

Crystal structure and chemical states

XRD analysis was carried out to determine the crystalline phases of the prepared samples. As depicted in Fig. 3a, the characteristic diffraction peaks of pure g-C_3N_4 at 13.0° and 27.4° were indexed to the (100) and (002) diffraction planes of g-C_3N_4 (JCPDS Card No. 87-1526), respectively. For the g-BN, two broad diffraction peaks located at around 26.9° and 42.2° were detected and were ascribed to the (002) and (100) crystal planes of BN (JCPDS Card No. 85-1068). No substantial difference in the diffraction patterns was recognized amongst the g-C_3N_4, 0.3% g-BN/g-C_3N_4, 0.6% g-BN/g-C_3N_4, 0.9% g-BN/g-C_3N_4, 1.2% g-BN/g-C_3N_4 and pure g-BN structures. These results suggest that the crystal structure and crystallization of g-C_3N_4 were not influenced by the fusion of g-BN possibly because of the minor content and smaller diffraction intensity of graphene-like BN. Moreover, the patterns did not show any other diffraction peaks that signify that as-obtained g-BN/g-C_3N_4 heterostructured photocatalysts are two-phase hybrids.

X-ray photoelectron spectroscopy (XPS), a sensitive analysis of the chemical state of a material surface, was used to investigate the chemical composition of g-BN/g-C_3N_4 composites. The high-resolution spectrum of B 1*s*, C 1*s*, O 1*s* and N 1*s* is depicted in Fig. 3b. The reference C 1*s* peak exhibited a binding energy at 284.8 eV. The C 1*s* spectrum of the g-BN/g-C_3N_4 material is shown in Fig. 3c. Clearly, the peak at 284.78 eV was due to carbon contamination on the exterior of g-BN/g-C_3N_4 composites. According to a prior report, the peaks at 287.88 and 288.26 eV have been assigned to N–C–N species in g-C_3N_4 [35]. The minor peak at 288.8 eV is attributed to sp^2-hybridized carbon that is attached to the NH_2 species in the triazine ring [36]. The N 1*s* spectrum of CN was deconvoluted into three peaks with binding energies at approximately 398.5, 399.2 and 400.6 eV, which were assigned to sp^2-hybridized pyridine nitrogen (C=N–C), graphitic N–C and tertiary nitrogen (N–C_3), respectively [36, 37]. Figure 3e depicts the B 1*s* signal, which was deconvoluted into two peaks due to B=C and B=N bonds at 190.8 and 191.7 eV, respectively. The O 1*s* spectrum of the g-BN/g-C_3N_4 hybrid structure is portrayed in Fig. 3f. The high-resolution XPS spectrum shows the O 1*s* core level at 532.6 eV, which is essentially due to absorbed water [38]. Two additional peaks were observed at 531.6 and 533.5 eV that correspond to N–C–O and C–OH species, respectively [39, 40].

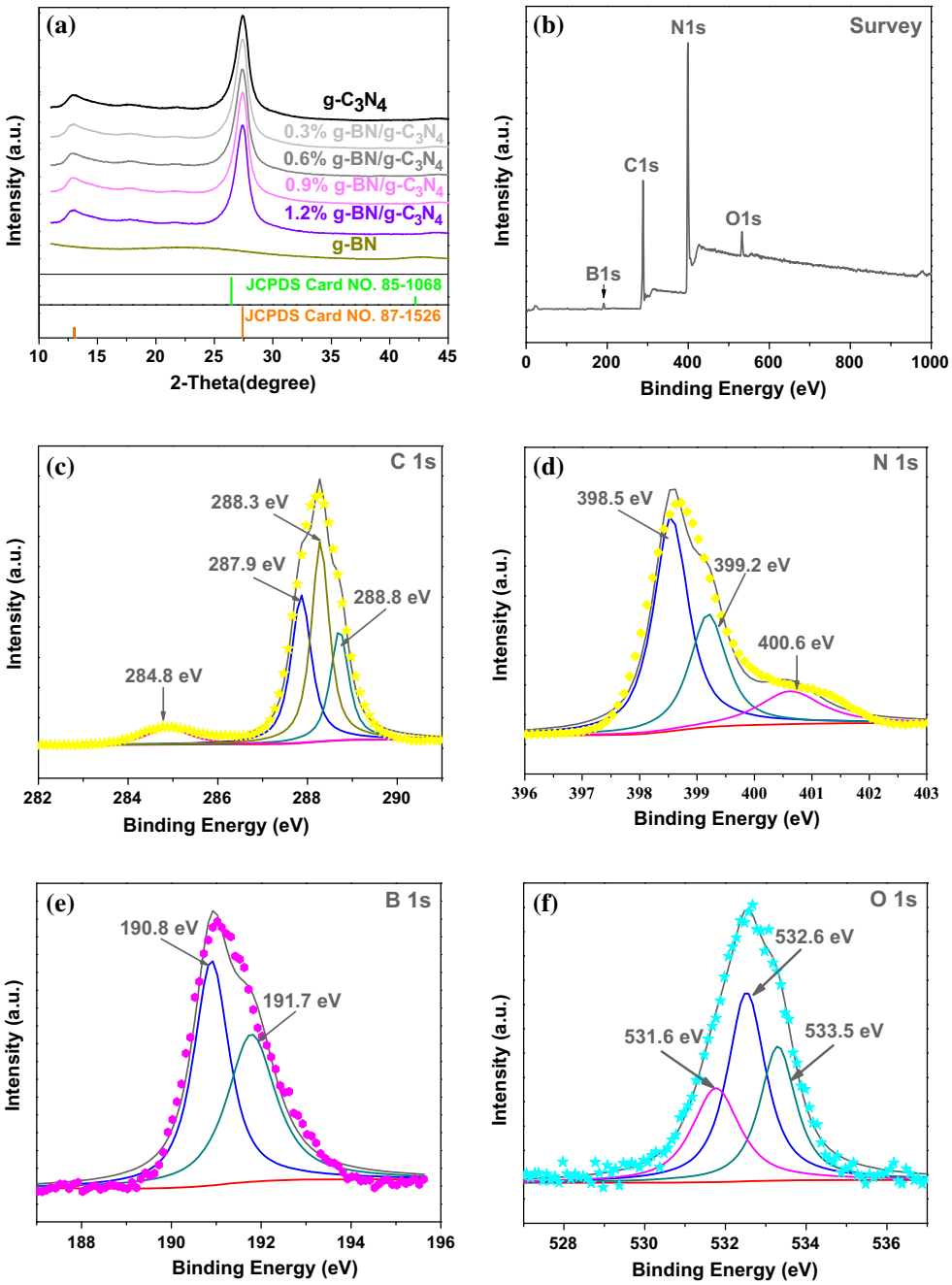

Figure 3 XRD patterns of as-prepared g-C_3N_4 and g-BN/g-C_3N_4 photocatalysts (**a**), XPS survey spectra (**b**) and high-resolution C 1*s* (**c**), N 1*s* (**d**), B 1*s* (**e**) and O 1*s* (**f**) of the 0.9% g-BN/g-C_3N_4 composites.

Photocatalytic activity

The photocatalytic activities of the samples were validated by the photocatalytic degradation of a BPA aqueous solution (10 mg L^{-1}) with visible-light. Figure 4a shows that after visible-light irradiation for 150 min, the degradation rates of BPA are 40.9, 59.8, 74.4, 91.9 and 84.4% in the presence of g-C_3N_4, 0.3% g-BN/g-C_3N_4, 0.6% g-BN/g-C_3N_4, 0.9% g-BN/g-C_3N_4 and 1.2% g-BN/g-C_3N_4, respectively. Moreover, 0.9% g-BN/g-C_3N_4 composites demonstrated the best performance, which was attributed to the fastest reduction rate of C/C_0 compared with the other samples.

Previous studies indicated [41] that the degradation of dyes may be due to a pseudo-first-order reaction using the following simplified Langmuir–Hinshelwood model at small C_0: In $(C_0/C) = kt$, where k is the apparent first-order rate constant. As presented in Fig. 4b, the equivalent pseudo-first-order rate constants for the photodegradation of BPA

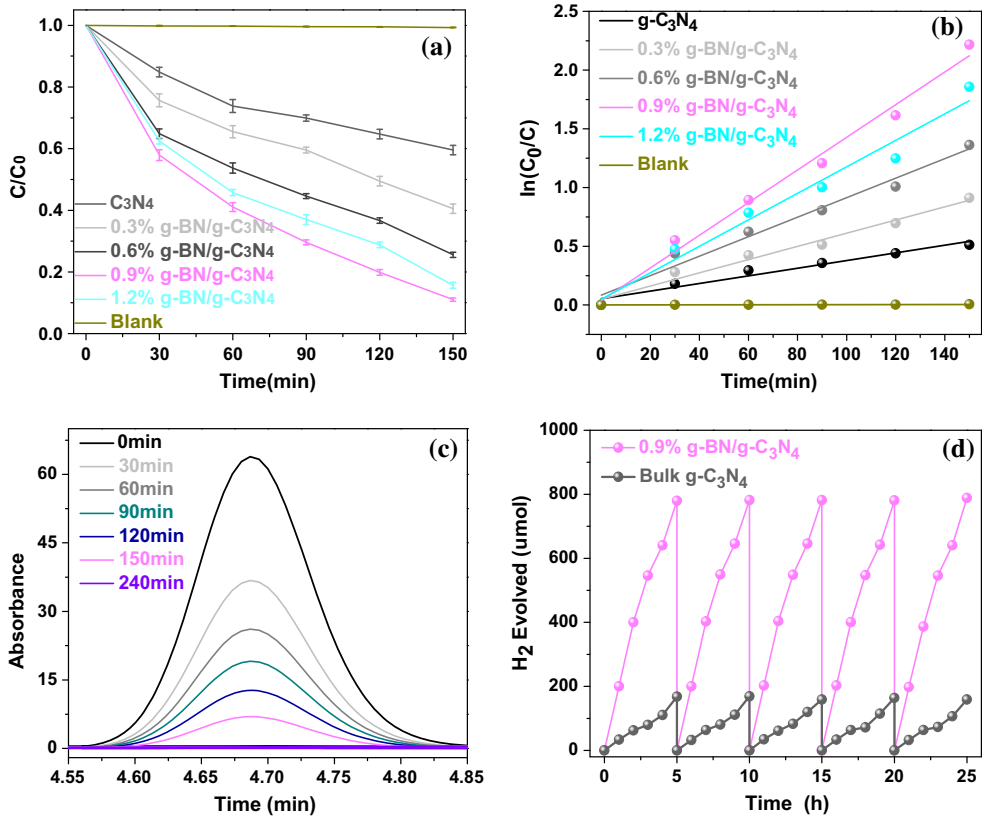

Figure 4 **a** Time profiles of the photocatalytic degradation of BPA samples under visible-light illumination with error bars ($\lambda > 420$ nm). **b** The corresponding selected fitting results using pseudo-first-order reaction kinetics. **c** HPLC chromatograms of extension of a time about 240 min during the photocatalytic degradation of BPA in aqueous solution. **d** Timeline of photocatalytic H_2 evolution.

for g-C_3N_4, 0.3% g-BN/g-C_3N_4, 0.6% g-BN/g-C_3N_4, 0.9% g-BN/g-C_3N_4 and 1.2% g-BN/g-C_3N_4 were calculated to be 0.00324, 0.00562, 0.00829, 0.01389 and 0.01126 min^{-1}, respectively. The heightened photocatalytic activity of the composites may be due to the charge transfer in g-BN during visible-light irradiation. In summary, when the g-BN content of g-BN/g-C_3N_4 ranges from 0.3 to 0.9%, g-BN successfully transferred photogenerated electrons from the conduction band of g-C_3N_4 and supplied more adsorptive BPA. However, the introduction of excess g-BN into g-C_3N_4 may block the pathway of visible-light irradiation, which leads to low light adsorption and a covering of the active sites that are beneficial to the photocatalytic reaction.

As portrayed in Fig. 4c, the characteristic absorption band of BPA at 4.68 min remarkably decreased with increasing irradiation time. These absorption peaks completely disappeared after 240 min of irradiation, which indicates the complete mineralization of the BPA solution. Figure S2 depicts the absorption spectra of aqueous solutions of BPA in various samples that were placed in darkness at room temperature. The adsorption properties of g-BN/g-C_3N_4 were significantly enhanced with an increase in g-BN content. This enhancement indicates that the combination of g-BN can improve the adsorption property of g-C_3N_4, which is consistent with the BET results.

To analyse the introduction of g-BN with g-C_3N_4 during the mineralization of BPA, TOC spectra of g-C_3N_4 and g-BN/g-C_3N_4 were evaluated. Figure S3 indicates that the change of graphene-like BN to graphene-like C_3N_4 has positively influenced the mineralization rate, which is in accordance with the above photocatalytic activity of various catalysts.

H_2 evolution by water splitting under visible-light irradiation was performed to assess the photocatalytic activity of the as-prepared composites. As illustrated in Fig. 4d, the 0.9% g-BN/g-C_3N_4 sample displays a noticeably higher photocatalytic hydrogen generation activity. The average H_2 evolution rate for the 0.9% g-BN/g-C_3N_4 sample reached 156 μmol h^{-1},

which is nearly 4.66 times that of pure g-C_3N_4 (33.5 μmol h^{-1}). Additionally, the stability of H_2 evolution for the 0.9% g-BN/g-C_3N_4 composite was assessed by iterating the photoreaction under similar conditions for five cycles. Evidently, no significant decrease in H_2 evolution rate was observed, which endorsed the supernal stability of g-C_3N_4 modified with graphene-like BN in the photocatalytic reaction.

Optical and electrochemical performance characterization

The UV–Vis diffuse reflectance spectra of the as-prepared samples are depicted in Fig. 5a. As demonstrated, pristine g-C_3N_4 showed adsorption wavelengths up to 460 nm, whereas pure BN exhibited an obvious adsorption in the visible-light region. Obviously, the g-BN/g-C_3N_4 samples have enhanced adsorption in the visible region. The observations indicate that the visible-light response is characteristic of these as-prepared photocatalysts. As portrayed in Fig. 5b, the band gaps of g-C_3N_4, 0.3% g-BN/g-C_3N_4, 0.6% g-BN/g-C_3N_4, 0.9% g-BN/g-C_3N_4 and 1.2% g-BN/g-C_3N_4 were estimated to be 2.59, 2.56, 2.50, 2.54 and 2.70 eV, respectively. Additionally, the band gap value is smaller when g-C_3N_4 was coupled with graphene-like BN, which indicates that more photoexcited electron–hole pairs may be produced with the same light intensity.

Transient photocurrent responses of the g-BN and g-BN/g-C_3N_4 electrodes were documented via five periodic on–off cycles of visible-light irradiation at a bias potential of 0.3 V. These experiments were performed to better comprehend and verify the mechanism of photocatalytic activity. An *i–t* curve was used to evaluate the photogenerated charge separation and transfer performance, which represents the charge collection effectiveness. Specifically, a sample with an elevated photocurrent value possessed a greater separation of electrons and holes [42]. Figure 5c shows that 0.9% g-BN/g-C_3N_4 has a higher photocurrent intensity compared with pure g-C_3N_4, which illustrates that 0.9% g-BN/g-C_3N_4 possessed a reduced recombination rate and better parting of photogenerated electron–hole pairs [43, 44]. Furthermore, the photocurrent was stable. This is because the graphene-analogue BN can modify the surface/interface photogenerated electron behaviour of the

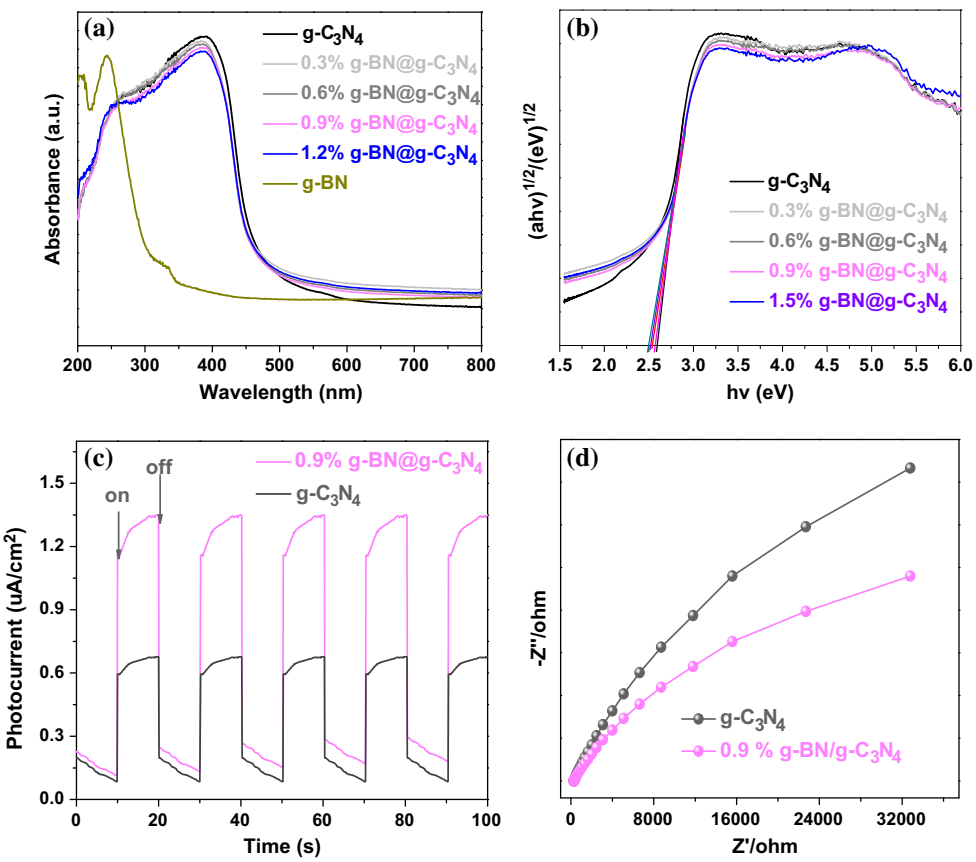

Figure 5 **a** UV–Vis spectra of various catalysts; **b** $(\alpha hv)^{1/2}$ versus hv curves of different catalysts. **c** Transient photocurrent responses of bulk g-C_3N_4 and 0.9% g-BN/g-C_3N_4. **d** EIS Nyquist plots of bulk g-C_3N_4 and 0.9% g-BN/g-C_3N_4.

photocatalyst and subdue the recombination of electron–hole pairs [45, 46]. The photocurrent response of the g-BN/g-C_3N_4 sample has also revealed another significant result. The late response of the as-obtained electrode indicates that g-BN collected the photoexcited electrons. The results are consistent with those from the previous report regarding carbon-based composites [47]. Upon light irradiation, g-BN worked like an electron pool that stored a portion of the photogenerated electrons, which resulted in the occurrence of a steadily increasing photocurrent response. Additionally, when the irradiation was switched off, the slow photocurrent discharge from g-BN resulted in a slow response in the photocurrent delay curve. These implications signal that there was improved photocarrier separation in the g-BN/g-C_3N_4 composite relative to pure g-C_3N_4. This describes, in part, the exceptionally higher photocatalytic activity of the composites [48].

The experimental Nyquist impedance plots for pristine C_3N_4 and 0.9% g-BN/g-C_3N_4 are presented in Fig. 5d to verify the enhanced interfacial charge transfer effect of g-BN/g-C_3N_4. The semicircle at high frequencies in the EIS diagrams reflects the charge transfer process at the photoelectrode interface. A less pronounced arc radius denotes a more proficient charge transfer process [49]. A much smaller semicircle was observed for 0.9% g-BN/g-C_3N_4, which indicates that the interfacial charge transfer occurred more quickly at the surface of g-BN/g-C_3N_4 compared with pristine g-C_3N_4. Hence, the incorporation of g-BN can effectively decrease the charge transfer resistance at the material surface [48]. This decrease is essentially due to improved electronic conductivity at the surface of 0.9% g-BN/g-C_3N_4 and is useful for the efficient parting of photogenerated electron–hole pairs.

Stability evaluation

The stability of the composite photocatalyst was investigated using recycle experiments with 0.9% g-BN/g-C_3N_4 catalysts under visible-light irradiation. The sample was amassed and cleaned with ultrapure water and absolute ethanol three times after each cycling test. Later, the as-prepared sample was dried in vacuum at 60 °C for 24 h for subsequent recycling and reuse. Figure 6a demonstrates that the photocatalytic activity did not decrease after five cycles, which indicates the high stability of the composite. XRD was employed to research the chemical stability of the 0.9% g-BN/g-C_3N_4 sample. Figure 6b clearly shows that there is no remarkable variation in the XRD pattern of the reused photocatalyst compared with the pattern of the as-prepared catalyst. These data imply that chemical structure of the 0.9% g-BN/g-C_3N_4 sample was stable throughout the photocatalytic reactions.

Photocatalytic mechanism

The separation efficiency of the photogenerated charge carriers in a semiconductor is frequently investigated using photoluminescence (PL) emission spectroscopy. The PL emission signal is due to the recombination of excited electrons and holes [42, 50]. The PL spectra of the as-synthesized samples (Fig. 7a) display an emission peak centred at ca. 445 nm (2.79 eV) under excitation at 325 nm (~3.82 eV) at room temperature. A low PL intensity usually denotes a reduced photogenerated electron–hole recombination rate. The g-BN/g-C_3N_4 composites showed significantly reduced PL intensities relative to bulk C_3N_4, which signified a significant drop

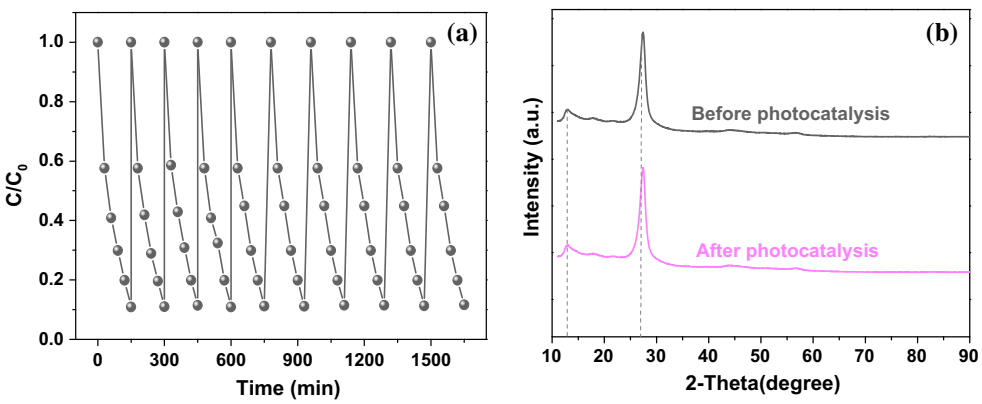

Figure 6 **a** Cycling photocatalytic experiments of 0.9% g-BN/g-C_3N_4 photocatalyst for the degradation of BPA under visible-light irradiation. **b** The XRD pattern of the 0.9% g-BN/g-C_3N_4 sample after the tenth run cycle photocatalytic experiment.

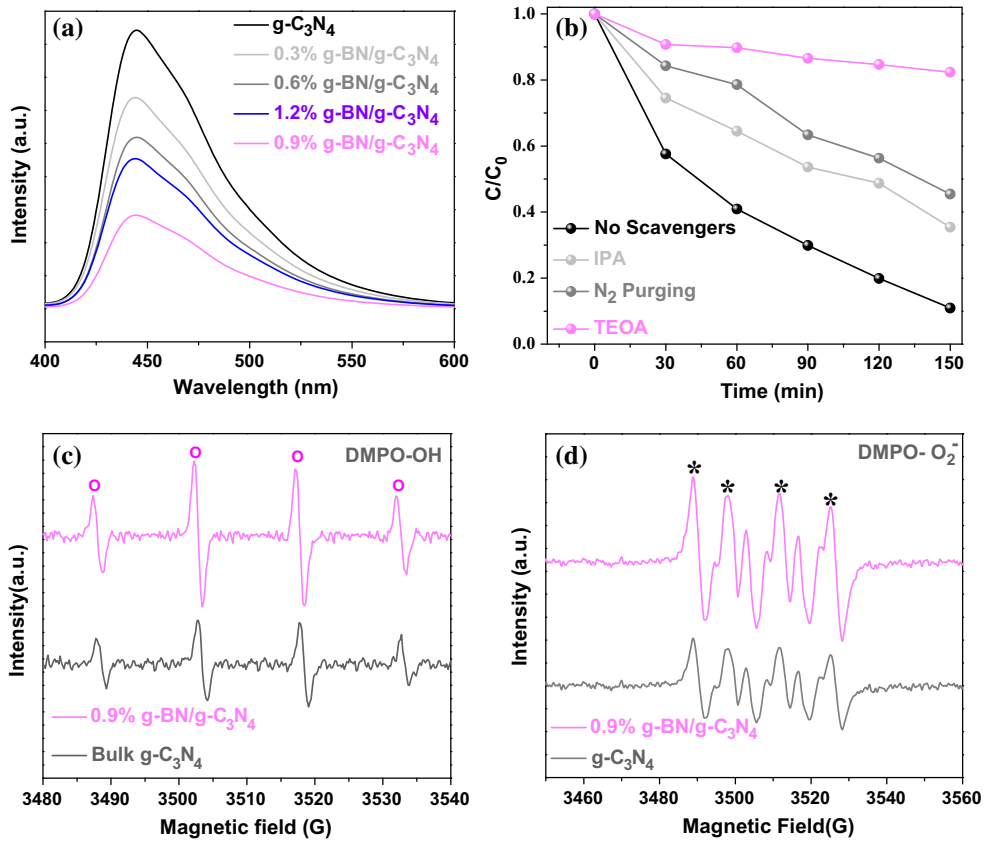

Figure 7 **a** Photoluminescence (PL) spectra of pure g-C_3N_4 and g-BN/g-C_3N_4 with different contents of g-BN. **b** Active species trapping experiments of the 0.9% g-BN/g-C_3N_4 photocatalyst under visible-light illumination. DMPO-ESR spin-trapping spectra of g-C_3N_4 and 0.9% g-BN/g-C_3N_4 composites for **c** hydroxide radicals (OH) in an aqueous dispersion and **d** super oxidations (O_2^-) in a methanol dispersion under visible-light irradiation for 120 s.

in charge recombination. The 0.9% g-BN/g-C_3N_4 composite showed the weakest intensity, which indicates an improved separation of photogenerated charge carriers. This result is consistent with the photocatalytic activity result and also means that the inclusion of g-BN can hamper the recombination.

Typically, photocatalysts with a higher BET surface area (S_{BET}) and greater total pore volume are conducive to an improved photocatalytic reaction because of the increase in the number of surface active sites that can rapidly absorb and mineralize the organic contaminant through the inter-associated porous structure and optimize the photocatalytic performance [51]. The textual information regarding the as-prepared 0.9% g-BN/g-C_3N_4 and pristine C_3N_4 samples was retrieved through nitrogen adsorption measurements. The nitrogen adsorption–desorption isotherms of 0.9% g-BN/gC_3N_4 and pristine C_3N_4 are shown in Fig. S4. On the basis of the IUPAC classification, all samples have similar type IIb adsorption–desorption isotherms, which indicates the presence of mesopores [50, 52, 53]. Using the linear part of the g-BN/g-C_3N_4 multipoint plot, the surface area was calculated to be 97.92 m^2/g, which is much higher than of C_3N_4 (13.86 m^2/g). Compared with pristine C_3N_4, the specific surface areas of the g-BN/g-C_3N_4 composites were significantly higher, which implies an enhancement in adsorption properties with the introduction of graphene-like BN into g-C_3N_4. In addition, the S_{BET}, average pore diameter and total pore volume of the samples are listed in supplementary Table 1.

Diverse active species trapping experiments for the mineralization of BPA in all the 0.9% g-BN/g-C_3N_4 composites were conducted to better comprehend the photocatalytic process. It was expected that a photocatalytic process involves many active species, including *OH, H^+ and $*O_2^-$. In this case, isopropanol (IPA), triethanolamine (TEOA) and N_2 purging were employed as *OH, H^+ and $*O_2^-$

scavengers, respectively. The photocatalytic activity of g-BN/g-C_3N_4 nanocomposites (shown in Fig. 7b) was greatly inhibited after TEOA fusion, which denotes that H^+ was the prime reactive species. Additionally, after IPA and N_2 purging, a decrease in photocatalytic activity was apparent, which means that *OH and $*O_2^-$ also have a significant role in the reaction process.

To identify *OH and $*O_2^-$ radicals in 0.9% g-BN/g-C_3N_4 photoreaction systems under visible-light irradiation, the ESR technique was employed. For bulk g-C_3N_4 and 0.9% g-BN/g-C_3N_4 composites, the four representative peaks of the DMPO-*OH radicals (Fig. 7c) and the six representative peaks of DMPO-O_2^- radicals (Fig. 7d) are apparent. These data signify that the *OH and $*O_2^-$ radicals are formed in both g-C_3N_4 and 0.9% g-BN/g-C_3N_4 reaction systems. Moreover, compared with bulk g-C_3N_4 sample, the *OH and $*O_2^-$ signal intensities of 0.9% g-BN/g-C_3N_4 sample were noticeably stronger relative to pristine g-C_3N_4, which means that the volume of *OH and $*O_2^-$ radicals produced on the 0.9% g-BN/g-C_3N_4 heterostructured surface is higher than that of pure g-C_3N_4. These results clearly indicate that $*O_2^-$ and *OH have a critical role in g-C_3N_4 and 0.9% g-BN/g-C_3N_4.

Therefore, the VB values of C_3N_4 (Fig. 8a) and g-BN (Fig. 8b) were measured by XPS valence spectroscopy. While the VB of g-BN (0.86 eV) is less positive to oxidize OH^- or H_2O to *OH for the standard reduction potential of $*OH/H_2O$ (2.27 eV) or $*OH/OH^-$ (2.38 eV). The CB value of sample is calculated by the formula $E_{CB} = E_{VB} - E_g$, where the E_g is the band gap and can be attained from the results of DRS. The photogenerated electrons in the conduction band (CB) of pure g-C_3N_4 reacted with O_2 to form $*O_2^-$ radicals because the position of the CB in g-C_3N_4 is more negative than the potential of $O_2/*O_2^-$ (−0.33 V vs. NHE). However, the valance band (VB) of g-C_3N_4 (1.63 eV vs. NHE) was less than the standard redox potential of *OH (2.72 V vs. NHE), which suggests that the photogenerated holes in the valence band of g-C_3N_4 cannot oxidize absorbed H_2O molecules to produce *OH. These observations suggest that *OH may be generated in the g-C_3N_4 photocatalytic system. Thus, *OH can be created by a further decrease in $*O_2^-$, which is a secondary means to generate *OH [54]:

$$e^- + O_2 \rightarrow {}^*O_2^- \quad (1)$$

$${}^*O_2^- + e^- + 2H^+ \rightarrow H_2O_2 \quad (2)$$

$${}^*O_2^- + H_2O \rightarrow {}^*OH + OH^- + O_2 \quad (3)$$

$$H_2O_2 \rightarrow 2{}^*OH \quad (4)$$

Next, the highly reactive radical species including $*OH, *O_2^-$ and H^+ participated in the photodecomposition process of the BPA aqueous solution. The primary processes in this photodegradation BPA method under visible-light irradiation are explained as follows.

$$g\text{-BN}/g\text{-}C_3N_4 + h\nu \rightarrow g\text{-BN}/g\text{-}C_3N_4(e^- + h^+) \quad (5)$$

$$g\text{-BN}/g\text{-}C_3N_4(e^- + h^+) \rightarrow g\text{-}C_3N_4(h^+) + g\text{-BN}(e^-) \quad (6)$$

$$g\text{-BN}(e^-) + O_2 \rightarrow {}^*O_2^- + {}^*OH \quad (7)$$

$${}^*O_2^-, h^+, {}^*OH + \text{BPA} \rightarrow \text{other products} \rightarrow CO_2 + H_2O \quad (8)$$

As per the abovementioned experimental results, the improved photocatalytic mechanism of g-BN/g-C_3N_4 materials was suggested and a schematic is shown in Fig. 9. Pure g-C_3N_4 absorbed light at wavelengths less than 470 nm. Additionally, the

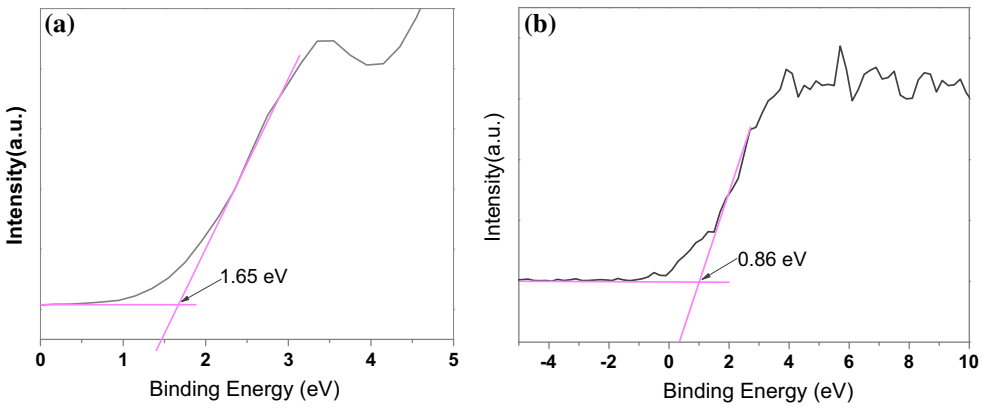

Figure 8 Valence band XPS spectra of the **a** C3N4 and **b** g-BN catalysts.

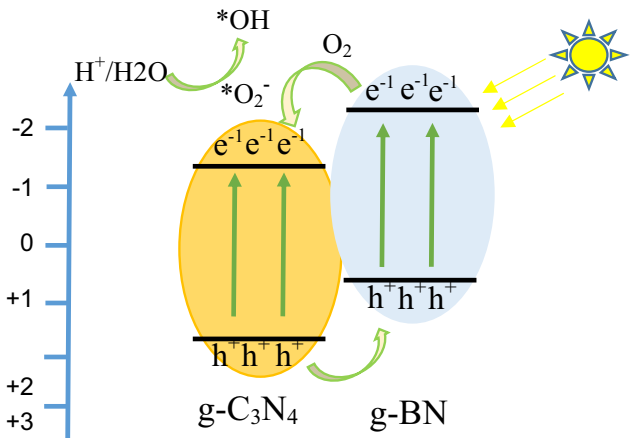

Figure 9 A possible photocatalytic mechanism in the g-BN/g-C_3N_4 nanocomposites under visible-light irradiation.

interfacial charge transfer effect between g-BN and graphitic carbon nitride facilitated a feasible shift of photogenerated electrons from g-C_3N_4 to g-BN. These processes greatly constrained the recombination of photogenerated electrons and holes. Therefore, the g-BN/g-C_3N_4 nanocomposite enhanced the charge generation by spreading the adsorption region towards visible-light wavelengths and also assisting charge parting and transport at the interface. In fact, g-BN has good electronic capture performance unless BN is helpful to prevent the rapid recombination of photoinduced electron–hole pairs of pure catalysts. This effect ultimately improved the number of photogenerated electrons and promoted their combination with adsorbed O_2 to produce active radicals by accelerating bisphenol A degradation.

Conclusions

We implemented a simple technique to prepare g-BN/g-C_3N_4 composites to reduce organic contaminants. The similar π–π conjugated structure of the g-C_3N_4 and g-BN components confirmed the creation of a tight junction in the g-BN/g-C_3N_4 materials. Because of an interfacial charge transfer effect that was enabled by the introduction of graphene-like BN (a large superficial area with more active sites and a better separation of photoelectrons and photoholes), the g-BN/g-C_3N_4 composite significantly enhanced biophenol A photodegradation and H_2 photoevolution with visible-light. This work will inspire new research in graphene-like BN-based photocatalysts and support their practical use in ecological conservation.

Acknowledgements

This work was supported by the National Natural Science Foundation of China (Nos. 51578209 and 51678213) and A Project Funded by the Priority Academic Program Development of Jiangsu Higher Education Institutions.

Electronic supplementary material: The online version of this article (doi:10.1007/s10853-017-1167-6) contains supplementary material, which is available to authorized users.

References

[1] Wang Y, Chen J, Xu Q, Li Y, Fu T, Jiang G, Li Y, Zhao Z, Wei Y (2017) Novel visible-light-driven S-doped carbon dots/BiOI nanocomposites: improved photocatalytic activity and mechanism insight. J Mater Sci 12:7282–7293. doi:10.1007/s10853-017-0965-1

[2] Zhou L, Zhang H, Sun H, Liu S, Moses O, Wang S, Jin W (2016) Recent advances in non-metal modification of graphitic carbon nitride for photocatalysis: a historic review. Catal Sci Technol 6:7002–7023

[3] Xu H, Wu Z, Ding M et al (2017) Microwave-assisted synthesis of flower-like BN/BiOCl composites for photocatalytic Cr(VI) reduction upon visible-light irradiation. Mater Des 114:129–138

[4] Wang X, Maeda K, Thomas A, Takanabe K, Xin G, Carlsson JM, Domen K, Antonietti M (2009) A metal-free polymeric photocatalyst for hydrogen production from water under visible light. Nat Mater 8:76–80

[5] Liu Q, Guo Y, Chen Z, Zhang Z (2016) Constructing a novel ternary Fe(III)/graphene/g-C_3N_4 composite photocatalyst with enhanced visible-light driven photocatalytic activity via interfacial charge transfer effect. Appl Catal B 183:231–241

[6] Leong KH, Liu SL, Sim LC, Saravanan P, Jang M, Ibrahim S (2015) Surface reconstruction of titania with g-C_3N_4 and Ag for promoting efficient electrons migration and enhanced visible light photocatalysis. Appl Surf Sci 358:370–376

[7] Feng QM, Shen YZ, Li MX, Zhang ZL, Zhao W, Xu JJ, Chen HY (2015) Dual-wavelength electrochemiluminescence ratiometry based on resonance energy transfer between Au nanoparticles functionalized g-C_3N_4 nanosheet and Ru(bpy)$^{32+}$ for microRNA detection. Anal Chem 88:937–944

[8] Li X, Li M, Yang J, Li X, Hu T, Wang J, Sui Y, Wu X, Kong L (2014) Synergistic effect of efficient adsorption g-C_3N_4/ZnO composite for photocatalytic property. J Phys Chem Solids 75:441–446

[9] Xu M, Han L, Dong S (2013) Facile fabrication of highly efficient g-C_3N_4/Ag_2O heterostructured photocatalysts with enhanced visible-light photocatalytic activity. ACS Appl Mater Interfaces 5:12533–12540

[10] Fagan R, McCormack DE, Hinder SJ, Pillai SC (2016) Photocatalytic properties of g-C_3N_4–TiO_2 heterojunctions under UV and visible light conditions. Materials 9:286–296

[11] Yin S, Di J, Li M, Sun Y, Xia J, Xu H, Fan W, Li H (2016) Ionic liquid-assisted synthesis and improved photocatalytic activity of pn junction g-C_3N_4/BiOCl. J Mater Sci 51:4769–4777. doi:10.1007/s10853-016-9746-5

[12] Liu D, Jiang Z, Zhu C, Qian K, Wu Z, Xie J (2016) Graphene-analogue BN-modified microspherical BiOI photocatalysts driven by visible light. Dalton Trans 45:2505–2516

[13] Sun J, Song J, Gondal M, Shi S, Lu Z, Xu Q, Chang X, Xiang D, Shen K (2015) Preparation of g-C_3N_4/BiOX (X = Cl, Br, I) composites, and their photocatalytic activity under visible light irradiation. Res Chem Intermed 41:6941–6955

[14] Hu JY, Ke T, Hong J (2016) Improvement of phenol photodegradation efficiency by a combined g-C_3N_4/Fe(III)/persulfate system. Chemosphere 148:34–40

[15] Sasaki Y, Iwase A, Kato H, Kudo A, Sasaki Y, Iwase A, Kato H, Kudo A (2008) The effect of co-catalyst for Z-scheme photocatalysis systems with an Fe^{3+}/Fe^{2+} electron mediator on overall water splitting under visible light irradiation. J Catal 259:133–137

[16] Guo SN, Min YL, Fan JC, Xu QJ (2015) Holey structured graphitic carbon nitride thin sheets with edge oxygen doping via photo-fenton reaction with enhanced photocatalytic activity. Appl Catal B 185:315–321

[17] Neto AC, Novoselov K (2011) New directions in science and technology: two-dimensional crystals. Rep Prog Phys 74:082501

[18] Han S, Hu L, Liang Z, Wageh S, Al-Ghamdi A, Chen Y, Fang X (2014) One-step hydrothermal synthesis of 2D hexagonal nanoplates of α-Fe_2O_3/graphene composites with enhanced photocatalytic activity. Adv Funct Mater 24:5719–5727

[19] Tian Q, Wu W, Liu J et al (2017) Dimensional heterostructures of 1D CdS/2D ZnIn 2 S 4 composited with 2D graphene: designed synthesis and superior photocatalytic performance. Dalton Trans 46:2770–2777

[20] Xu Y, Xu H, Wang L, Yan J, Li H, Song Y, Huang L, Cai G (2013) The CNT modified white C_3N_4 composite photocatalyst with enhanced visible-light response photoactivity. Dalton Trans 42:7604–7613

[21] Liao G, Chen S, Quan X, Yu H, Zhao H (2012) Graphene oxide modified g-C_3N_4 hybrid with enhanced photocatalytic capability under visible light irradiation. J Mater Chem 22:2721–2726

[22] Tong Z, Yang D, Shi J, Nan Y, Sun Y, Jiang Z (2015) Three-dimensional porous aerogel constructed by g-C_3N_4 and graphene oxide nanosheets with excellent visible-light photocatalytic performance. ACS Appl Mater Interfaces 7:25693–25701

[23] Deng Y, Liu K, Cao H, Luo M, Yan H (2015) Synthesis of graphene with both high nitrogen content and high surface area by annealing composite of graphene oxide and g-C_3N_4. J Iran Chem Soc 12:807–814

[24] Gannett W, Regan W, Watanabe W, Taniguchi T, Crommie M, Zettl A (2011) Boron nitride substrates for high mobility chemical vapor deposited graphene. Appl Phys Lett 98:242–255

[25] Kim KK, Hsu A, Jia X, Kim SM, Shi Y, Dresselhaus M, Palacios T, Kong J (2012) Synthesis and characterization of hexagonal boron nitride film as a dielectric layer for graphene devices. ACS Nano 6:8583–8590

[26] Kiran M, Raidongia K, Ramamurty U, Rao C (2011) Improved mechanical properties of polymer nanocomposites incorporating graphene-like BN: dependence on the number of BN layers. Scr Mater 64:592–595

[27] Li TL, Hsu SLC (2010) Enhanced thermal conductivity of polyimide films via a hybrid of micro-and nano-sized boron nitride. J Phys Chem B 114:6825–6829

[28] Shin H, Guan J, Zgierski MZ, Kim KS, Kingston CT, Simard B (2015) Covalent functionalization of boron nitride nanotubes via reduction chemistry. ACS Nano 9:12573–12582

[29] Ding S, Mao D, Yang S et al (2017) Graphene-analogue h-BN coupled Bi-rich Bi4O5Br 2 layered microspheres for enhanced visible-light photocatalytic activity and mechanism insight. Appl Catal B 2:1213–1258

[30] Liu D, Zhang M, Xie W, Sun L, Chen Y, Lei W (2017) Porous BN/TiO_2 hybrid nanosheets as highly efficient visible-light-driven photocatalysts. Appl Catal B 207:72–78

[31] Chen Z, Chen X, Di J, Liu Y, Yin S, Xia J, Li H (2017) Graphene-like boron nitride modified bismuth phosphate materials for boosting photocatalytic degradation of enrofloxacin. J Colloid Interface Sci 492:51–60

[32] Dai K, Lu L, Liu Q, Zhu G, Wei X, Bai J, Xuan L, Wang H (2014) Sonication assisted preparation of graphene oxide/-graphitic-C3N4 nanosheet hybrid with reinforced photocurrent for photocatalyst applications. Dalton Trans 43:6295–6299

[33] Wu W, Lv X, Wang J, Xie J (2017) Integrating AgI/AgBr biphasic heterostructures encased by few layer h-BN with enhanced catalytic activity and stability. J Colloid Interface Sci 496:434–445

[34] Silva ESD, Prevot V, Forano C, Wong-Wah-Chung P, Burrows HD, Sarakha M (2014) Heterogeneous photocatalytic degradation of pesticides using decatungstate intercalated macroporous layered double hydroxides. Environ Sci Pollut R 21:11218–11227

[35] Ferencz Z, Szabados M, Ádok-Sipiczki M, Kukovecz A, Kónya Z, Sipos P, Pálinkó I (2014) Mechanochemically assisted synthesis of pristine Ca(II) Sn(IV)-layered double hydroxides and their amino acid intercalated nanocomposites. J Mater Sci 49:8478–8486. doi:10.1016/j.jssc.2015.10.038

[36] Fettkenhauer C (2015) Facile synthesis of new, highly efficient SnO_2/carbon nitride composite photocatalysts for the hydrogen evolution reaction. Green Chem 17:3350–3361

[37] Li XH, Zhang J, Chen X, Fischer A, Thomas A, Antonietti M, Wang X (2011) Condensed graphitic carbon nitride nanorods by nanoconfinement: promotion of crystallinity on photocatalytic conversion. Chem Mater 23:4344–4348

[38] Nag A, Raidongia K, Hembram KP, Datta R, Waghmare UV, Rao C (2010) Graphene analogues of BN: novel synthesis and properties. ACS Nano 4:1539–1544

[39] Clayton C, Lu Y (1986) A bipolar model of the passivity of stainless steel: the role of Mo addition. J Electrochem Soc 133:2465–2473

[40] Li HJ, Sun BW, Sui L, Qian DJ, Chen M (2015) Preparation of water-dispersible porous g-C_3N_4 with improved photocatalytic activity by chemical oxidation. Phys Chem Chem Phys 17:3309–3315

[41] Meng F, Zhang X, Xu B, Yue S, Guo H, Luo Y (2011) Alkali-treated graphene oxide as a solid base catalyst: synthesis and electrochemical capacitance of graphene/carbon composite aerogels. J Mater Chem 21:18537–18539

[42] Wang XJ, Yang WY, Li FT, Xue YB, Liu RH, Hao YJ (2013) In situ microwave-assisted synthesis of porous N–TiO_2/g-C_3N_4 heterojunctions with enhanced visible-light photocatalytic properties. Ind Eng Chem Res 52:17140–17150

[43] Zhou Y, Zhang L, Huang W, Kong Q, Fan X, Wang M, Shi J (2016) N-doped graphitic carbon-incorporated g-C_3N_4 for remarkably enhanced photocatalytic H_2 evolution under visible light. Carbon 99:111–117

[44] Karbhal I, Devarapalli RR, Debgupta J, Pillai VK, Ajayan PM, Shelke MV (2016) Facile green synthesis of BCN nanosheets as high-performance electrode material for electrochemical energy storage. Chem Eur J 22:7134–7140

[45] Li T, Zhao L, He Y, Cai J, Luo M, Lin J (2013) Synthesis of g-C_3N_4/$SmVO_4$ composite photocatalyst with improved visible light photocatalytic activities in RhB degradation. Appl Catal B 129:255–263

[46] Prakash A, Todi V, Sundaram KB, Ross L, Xu G, French M, Henry P, King SW (2015) Investigation of the dielectric and mechanical properties for magnetron sputtered BCN thin films. J Solid State Sci Technol 4:3122–3126

[47] Xu H, Yan J, Xu Y, Song Y, Li H, Xia J, Huang C, Wan H (2013) Novel visible-light-driven AgX/graphite-like C_3N_4 (X = Br, I) hybrid materials with synergistic photocatalytic activity. Appl Catal B 129:182–193

[48] Wang K, Li Q, Liu B, Cheng B, Ho W, Yu J (2015) Sulfur-doped g-C_3N_4 with enhanced photocatalytic CO_2-reduction performance. Appl Catal B 176:44–52

[49] Sun Q, Lv K, Zhang Z, Li M, Li B (2015) Effect of contact interface between TiO_2 and g-C_3N_4 on the photoreactivity of g-C_3N_4/TiO_2 photocatalyst:(001) vs (101) facets of TiO_2. Appl Catal B 164:420–427

[50] Dong G, Ho W, Li Y, Zhang L (2015) Facile synthesis of porous graphene-like carbon nitride ($C_6N_9H_3$) with excellent photocatalytic activity for NO removal. Appl Catal B 174:477–485

[51] Yu J, Ran J (2011) Facile preparation and enhanced photocatalytic H_2-production activity of $Cu(OH)_2$ cluster modified TiO_2. Energy Environ Sci 4:1364–1371

[52] Hong Y, Jiang Y, Li C, Fan W, Yan X, Yan M, Shi W (2016) In-situ synthesis of direct solid-state Z-scheme V_2O_5/g-C_3N_4 heterojunctions with enhanced visible light efficiency in photocatalytic degradation of pollutants. Appl Catal B 180:663–673

[53] Rokhsat E, Akhavan O (2016) Improving the photocatalytic activity of graphene oxide/ZnO nanorod films by UV irradiation. Appl Surf Sci 371:590–595

[54] Ghafuri H, Movahedinia Z, Rahimi R, Zand HRE (2015) Synthesis of 5, 10, 15, 20-tetrakis [4-(naphthalen-2-yloxycarbonyl) phenyl] porphyrin (TNBP) and its complexes with zinc and cobalt and an investigation of the photocatalytic activity of nano Fe_3O_4/ZrO_2–TNBP. RSC Adv 5:60172–60178